JOURNAL OF THE AMERICAN CHEMICAL SOCIETY

Article

pubs.acs.org/JACS

# Formation Mechanism of Silver Nanoparticles Stabilized in Glassy Matrices

Anne Simo,[†] Jörg Polte,[†] Norbert Pfänder,[‡] Ulla Vainio,[§] Franziska Emmerling,[#] and Klaus Rademann*,[†]

[†]Department of Chemistry, Humboldt-Universität zu Berlin, Brook-Taylor-Straße 2, 12489 Berlin, Germany
[‡]Department of Inorganic Chemistry, Fritz-Haber Institut, Faradayweg 4-6, 14195 Berlin, Germany
[§]HASYLAB at DESY, Notkestraße 85, 22607 Hamburg, Germany
[#]BAM Federal Institute of Materials Research and Testing, Richard-Willstätter-Straße 11, 12489 Berlin, Germany

*Supporting Information*

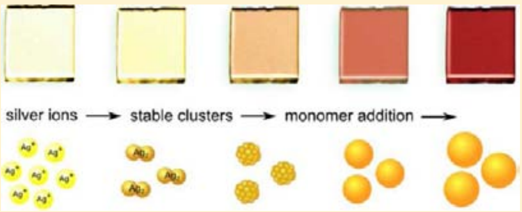

**ABSTRACT:** In any given matrix control over the final particle size distribution requires a constitutive understanding of the mechanisms and kinetics of the particle evolution. In this contribution we report on the formation mechanism of silver nanoparticles embedded in a soda-lime silicate glass matrix. For the silver ion-exchanged glass it is shown that at temperatures below 410 °C only molecular clusters (diameter <1 nm) are forming which are most likely silver dimers. These clusters grow to nanoparticles (diameter >1 nm) by annealing above this threshold temperature of 410 °C. It is evidenced that the growth and thus the final silver nanoparticle size are determined by matrix-assisted reduction mechanisms. As a consequence, particle growth proceeds after the initial formation of stable clusters by addition of silver monomers which diffuse from the glass matrix. This is in contrast to the widely accepted concept of particle growth in metal−glass systems, in which it is assumed that the nanoparticle formation is predominantly governed by Ostwald ripening processes.

## INTRODUCTION

Noble metal nanoparticles are one of the most intensively studied nanoscale materials due to their unique properties which make them attractive to numerous promising applications in medicine,[1,2] biotechnology,[3,4] catalysis,[5,6] and optoelectronics.[7,8] The favored applications require defined properties, which are in general determined by the particle size and shape, the interparticle distance, volume concentration, and chemical composition. To obtain the demanded nanoparticles in the desired matrix (solution, gel, glass, etc.), a profound understanding of the underlying mechanism of particle formation is essential. In recent publications, we were able to determine fundamental growth mechanisms for several colloidal metal nanoparticle syntheses.[9−11]

Due to its homogeneity, transparency, and solubility properties, soda-lime silicate glass is excellently suited as a matrix for fundamental research which requires minimal chemical interaction between the clusters and the host matrix. Moreover, glass matrices provide long-term stability of metal nanoparticles and smaller clusters. In glass even the smallest metal clusters can be stabilized and investigated.[12,13]

The history of gold−ruby glasses which contain also silver nanoparticles goes back to the Roman Empire. Silver-stained glasses are known since the early 14th century. The first datable example of silver-containing glasses are windows in the parish church of Le Mesnil-Villeman, France (1313)[14] The first known written report about the fabrication of noble metal-containing glasses was published in 1689 by Johannes Kunckel.[15]

Composite materials containing noble metal nanoparticles have attracted enormous attention in the last years due to novel photonic media in optoelectronics or for nonlinear optics.[16−18] Metal nanoparticles in glasses are considered with extensive interest for optical switching and filtering[19,20] and as high-capacity optical recording media.[21]

Advanced applications demand a well-defined particle size. So far, precise size control has not been straightforward for any kind of metal−glass system, and the problem of size-controlled synthesis is not solved yet. The knowledge of the mechanism that governs the growth is the prerequisite to improve nanoparticle syntheses in glass matrices. This demands experimental information about the particle size and concentration at the different stages of the synthetic procedure.

Common routes to generate metal nanoparticles in glass systems are the melt−quench technique,[22,23] sol−gel methods,[24,25] ion implantation,[26−28] and the ion-exchange method.[29−31] Among these methods the ion exchange is favorable in different aspects: (i) it is very efficient for the introduction of very high concentrations of metal ions, (ii) the glass remains intact (unlike the ion implantation technique, which introduces high damage in the glass matrix), and (iii) it can easily be upscaled which enables mass production of composite materials

**Received:** September 11, 2012
**Published:** October 25, 2012

containing metal nanoparticles. In addition, this method allows theoretically the separation of the ion-insertion process from the growth which can be essential for particle size control. Therefore, the ion-exchange method was chosen to introduce the metal species into the glass matrix. Soda-lime silicate glass was used which is the best-known and most investigated example of an engineered amorphous solid.[32] Recently, the structure of silicate glass could be identified on the atomic scale.[33] Ion-exchanged glasses are routinely used for glass strengthening[34] and gradient waveguide fabrication.[35,36] The ion-exchange method leads to a gradient silver ion concentration and is used for surface modification of the glass. The high silver ion concentration in the close vicinity of the glass surface can play an important role for sensor applications.[37,38] Recently, we demonstrated that low concentrations of biomolecules can be detected on silver ion-exchanged glasses using surface-enhanced Raman scattering (SERS).[39]

In this contribution the growth of silver nanoparticles in soda-lime silicate glass is investigated. Samples were prepared by a combined chemical and thermal treatment consisting of two steps: (1) metal ion introduction and (2) subsequent thermal treatment. This synthesis procedure separates the ion-insertion process from the actual particle growth. The particle formation is initiated by thermal treatment. Experiments were made on two sets of samples, which were prepared by either: (i) annealing of ion-exchanged samples at different temperatures or (ii) annealing of ion-exchanged samples at constant temperature for different periods of time. A schematic illustration of the sample preparation is depicted in Figure 1.

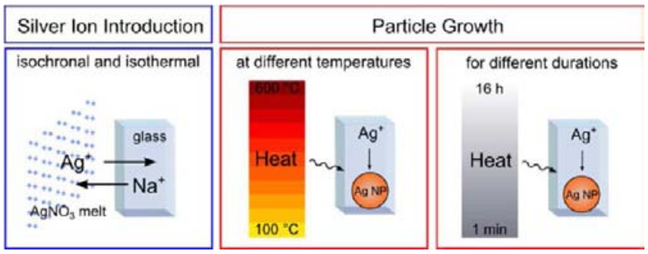

**Figure 1.** Schematic illustration of the sample preparation.

## RESULTS AND DISCUSSION

Each single step of the sample preparation, and thus particle formation, was investigated by combined experiments using small-angle X-ray scattering (SAXS), transmission electron microscopy (TEM), and optical absorption and emission spectroscopy. In addition, anomalous small-angle X-ray scattering (ASAXS) was used to support the interpretation of the SAXS data. These methods provide information about particles sizes and concentrations as well as the corresponding optical properties. From the combined experiments the mechanism of the silver nanoparticle formation in soda-lime silicate glass is deduced. In this contribution the notation "clusters" is used for particles with diameters ($d$) less than 1 nm.

**Ion-exchange.** Silver ions were introduced into the glass by immersing the glass slides into a bath of a molten salt mixture of $AgNO_3/NaNO_3$ (1:2). Sodium ions from the surface and the subsurface region of the glass are substituted by the silver ions. Extended ion-exchange duration leads to an increased penetration depth. Depth profiles were recorded with energy dispersive X-ray spectroscopy (EDX) from the cross sections of silver ion-exchanged glasses (Figure 2). The total amount of silver introduced into the glass corresponds to:[40]

$$M_t = 2C_0(D_T t/\pi)^{1/2} \tag{1}$$

where $C_0$ represents the surface concentration, $D_T$ the temperature dependent diffusion coefficient of silver ions and $t$ the duration of ion-exchange. The area under the concentration profile curve corresponds to the total amount of silver $M_t$. For the following investigations silver ion exchange was carried out for 60 min at 360 °C which leads to an average amount of silver of 9.75 wt % in a silver-containing layer of ~30 μm.

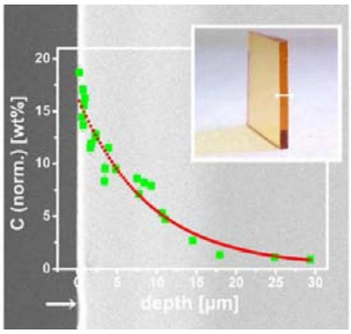

**Figure 2.** Cross-sectional ESEM picture (background image) and corresponding silver concentration profile of the ion-exchanged glass (green dots), recorded with EDX analysis. The recorded concentration profile was fitted using an exponential curve fit (red line). For EDX analysis the silver ion-exchanged sample was prepared in the cross-sectional profile (shown in the inset).

After 60 min of ion exchange, the samples are pale-yellow and remain transparent. The ion-exchanged samples show a slight absorption below 320 nm (Figure 3a). This absorption arises most likely from small silver clusters. Several cluster sizes are known to absorb in that UV range: $Ag_6$ and $Ag_{60}$ clusters in a He matrix absorb between 320 and 344 nm;[41] $Ag_2$, $Ag_3$, and $Ag_4$ in an Ar matrix at 227 and 261 nm, 245 nm, and 273 and 283 nm, respectively;[42] $Ag_1$−$Ag_4$,[43] $Ag_6$ and $Ag_8$,[44] and $Ag_7$[7] clusters in aqueous solution at around 260, 324, 347, and 350 nm, respectively. Furthermore, glass defects such as trapped electrons could contribute to the observed UV band.[45,46] However, the ion-exchanged samples show no plasmon resonance coming from silver nanoparticles (around 400 nm).

The silver ion-exchanged glass samples exhibit a green luminescence at an excitation wavelength ($\lambda_{exc}$) of 337 nm. The emission ranges from 400 to 800 nm (Figure 3b) with distinct maxima at 485, 521, 560, and 611 nm, and an additional shoulder at 670 nm. For the maximum at 560 nm a photoluminescence excitation (PLE) spectrum was recorded (see Figure S1 in the Supporting Information). This excitation spectrum ranges from 250 to 450 nm and exhibits two prominent maxima at 355 and 395 nm and an additional shoulder at 300 nm. The observed luminescence could originate from small silver clusters. Several publications describe the fluorescence of small silver clusters ($Ag_2$−$Ag_{12}$) with similar PL maximum peaks and absorption features.[7,47−50] These observations are slightly different from the fluorescence of the silver clusters in the glass matrix. The PL obtained for the silver ion-exchanged glasses match perfectly with those reported for gold clusters in soda-lime silicate glasses by

Eichelbaum et al.[51] The range, shape, and maximum position of the reported luminescence of the glass containing gold clusters is identical to our measurements. The superimposed PL spectra of a gold and silver glass is shown in Figure S2 in the Supporting Information.

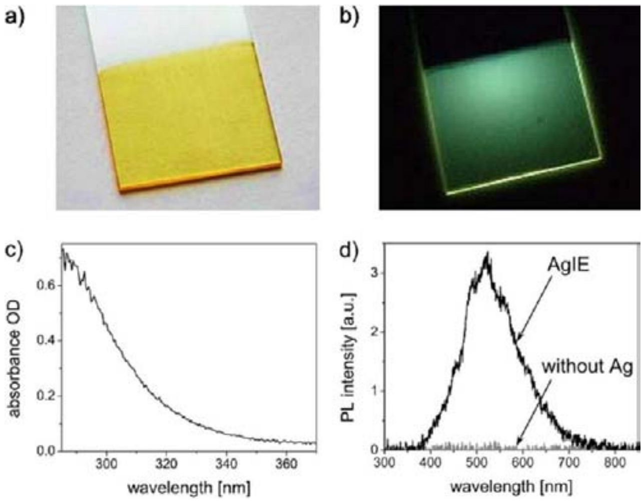

**Figure 3.** Photograph of (a) the ion-exchanged glass with pale-yellow color and (b) of the green luminescence under $\lambda_{exc}$ = 337 nm excitation. (c) Absorption spectrum of the ion-exchanged glass. (d) PL spectrum recorded with $\lambda_{exc}$ = 337.1 nm.

Moreover, the PL lifetime of the gold-containing glass, $\tau = 30$ $\mu$s, is in perfect agreement with our measurements for the silver glass, $\tau = 29.5$ $\mu$s (see Figure S3 in the Supporting Information). Thus, the observed luminescence has most likely the same origin and is related to the glass matrix. Besides the microsecond component also a nanosecond decay for silver clusters has been reported, indicating that multiple types of emissive species are present[52−54]In the gold-containing glass the observed luminescence was attributed to the glass-intrinsic luminescence center, abbreviated as the L-center.[51] The L-center consists of a silanolate unit with a sodium ion bound to the lone pair of one of the oxygens (nonbridging oxygen, NBO).[55] In the gold containing soda-lime silicate glasses the L-center emission is activated by metallic clusters.[51] The gold clusters, absorbing the UV light (337 nm), act as donors in a resonance energy transfer process toward the L-center. In the PLE spectrum of the gold containing glass three maxima at 240 nm, 300 nm, and 340 nm can be identified whereas the silver containing glasses show maxima at 300 nm, 355 nm, 395 nm. This difference between the PLE spectra is characteristic for an energy transfer process since the excitation spectrum is assigned to the absorption of the donor species. Consequently, the observed luminescence originates most likely from an energy transfer to the L-center from molecular silver clusters[56] ($N \leq$ 10) as the absorbing centers.

SAXS and ASAXS measurements of the 60-min ion-exchanged sample reveal that small structures with less than 1 nm in diameter are present (Figure 4a). For comparison a SAXS curve of fullerene ($C_{60}$) in toluene is shown. Fitting a spherical form factor[57] to the fullerene scattering curve exhibits a size of 0.8 nm in diameter. The curve shape of the silver sample is similar to this obtained for fullerenes, indicating that very small structures associated with silver are present. The curve shape indicates that these silver structures are smaller than the size of a fullerene. A fit of the scattering curve of the silver ion-exchanged sample with a spherical form factor of hard spheres reveals an average size of 0.6 nm in diameter. However, small differences in this size regime are difficult to determine and the size of the silver structures can be estimated to 0.6 ± 0.1 nm in diameter. ASAXS measurements show unambiguously that these structures originate from silver (see Figure 4b). The ASAXS measurements were performed at three different photon energies, below and at the Ag absorption K-edge (25516 eV). The scattering curves measured at 25509 eV (highest energy, E3) and at 25051 eV (lowest energy, E1) are shown in Figure 4b. The difference of these scattering curves reveals the contribution of silver to the scattering. Despite the low statistical accuracy the difference curve has approximately the same shape as the standard SAXS curves which are therefore caused by scattering from silver.

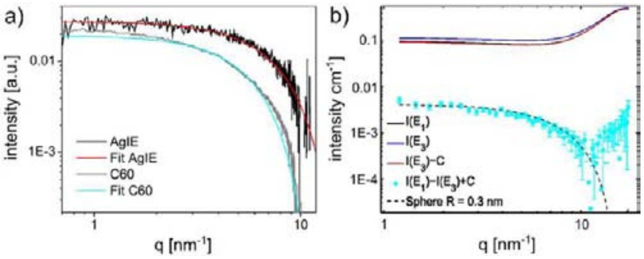

**Figure 4.** (a) SAXS curve of the ion-exchanged glass (AgIE) and the fit to this curve. For comparison the scattering curve with the corresponding fit of fullerenes (C60) in toluene is included. (b) ASAXS curves recorded at 25509 eV (E3) and 25051 eV (E1) and their difference for the ion-exchanged glass. The constant ($C = 0.21$) accounts for fluorescence background correction. Also a scattering from a theoretical form factor of a sphere of radius $R = 0.3$ nm is shown (dashed line).

The findings for the ion-exchange step are: (i) structures with dimensions of $<1$ nm in diameter are present in the glass (SAXS), (ii) these structures originate from silver (ASAXS), (iii) the characteristic silver nanoparticle plasmon band is not observed in the absorption spectra, and (iv) the samples luminesce weakly. The small silver entities with diameters of about 0.6 nm, which was determined with (A)SAXS, could be small silver clusters, silver ions or silver ion aggregates.[58]The PL intensity of the ion-exchanged samples is weak and increases when more clusters are formed during annealing (see Figure 5). Therefore it can be concluded that after ion exchange the majority of silver is present in the form of silver ions which do not contribute to the luminescence. The predominant presence of silver ions in ion-exchanged glasses has been observed by several groups. As reported by the groups of Yang et al., Dubiel et al., and Houde-Walter et al. from EXAFS experiments the size of the silver structures determined with SAXS fits to single silver ions in their oxygen coordination sphere or silver ion pairs.[59−61]

As a result, the ion-exchanged glasses contain primarily silver ions but also few clusters as deduced from the PL measurements. The cluster formation indicates that parts of the silver ions must have been reduced during the ion-exchange process at 360 °C.

**Annealing at Different Temperatures.** As depicted in Figure 1 the ion-exchanged samples were annealed to initiate the silver particle formation. In this section the influence of annealing temperature on the particle growth is examined. The

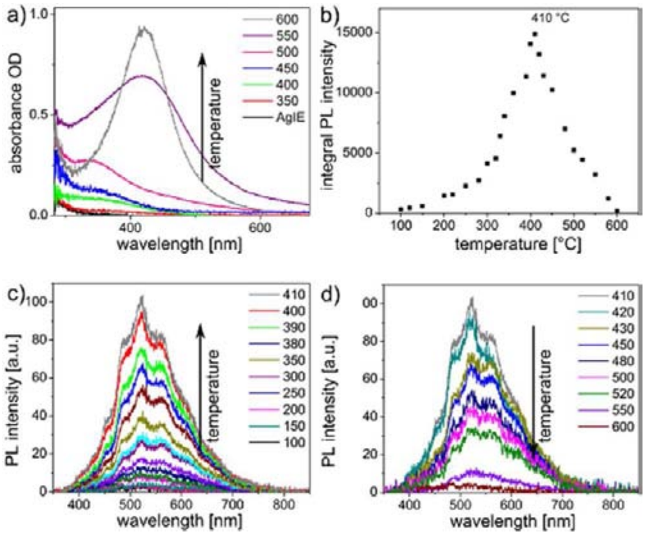

**Figure 5.** (a) Absorption spectra and (b) integral PL intensity of silver samples annealed at different temperatures. (c) PL spectra of silver samples annealed at 100−410 °C and (d) 410−600 °C. The legend is displayed only for selected PL spectra.

growth was studied in a temperature range of 100−600 °C with an annealing time of 30 min.

Absorption spectra were recorded for samples annealed at different temperatures in steps of 50 °C (see Figure 5a). Annealing the silver glass samples below 400 °C leads to a slight increase of the absorbance below 350 nm which can be attributed to small silver clusters ($d < 1$ nm).[7,41−44] During annealing with temperatures above 400 °C the absorbance at around 400 nm emerges. With increasing annealing temperature, this absorption band around 400 nm continuously increases. At 550 °C this band can clearly be assigned to the silver plasmon resonance at around 400 nm. At 600 °C the absorption band is increased and significantly narrower, with the maximum absorption at 420 nm.

Photoluminescence measurements were conducted for the annealed silver−glass samples. The PL measurements were carried out in steps of 10 °C. As measured for the ion-exchanged samples the PL emission ranges from 400 to 800 nm with distinct maxima at 485, 521, 560, and 611 nm and an additional shoulder at 670 nm (Figure 5c). The PL intensity doubles compared to that of the ion-exchanged sample when the samples are annealed for 30 min at 100 °C. With increasing annealing temperature, the PL intensity increases, reaching the maximum intensity at 410 °C, at which the intensity is increased by a factor of 30. At temperatures above the threshold temperature the PL intensity decreases abruptly and vanishes with further increase of the temperature (see Figure 5d). The intensity ratio of the four maxima remains nearly unchanged. Consequently, the decrease of the integrated PL intensity (400−800 nm) is accompanied by a decrease of all band features. Figure 5b shows the integral intensity as a function of temperature between 100 and 600 °C. The maximum intensity is found at 410 °C. This emphasizes that the concentration of emitting species increases below and decreases above the threshold temperature of 410 °C.

SAXS measurements were carried out in steps of 100 °C below and in steps of 50 °C above 400 °C annealing temperature. In accordance with the absorption and PL measurements, the SAXS investigations also reveal that nanoparticles are forming above the threshold temperature between 400 and 450 °C (see Figure 6a). At temperatures below the threshold the scattering curves are similar to the scattering curve obtained for the ion-exchanged sample. The scattering attributed to small silver structures (scattering at higher $q$-vectors, above 4 $\mathrm{nm}^{-1}$) persists even after the annealing above the threshold temperature. From the intensity increase at scattering vectors below 2 $\mathrm{nm}^{-1}$ it can be deduced that nanoparticles are forming. Consequently, for these samples with annealing temperature above 400 °C, silver nanoparticles as well as the small silver structures contribute to the scattering curve. The scattering of both species is sufficiently separated so that the scattering curves can be fitted using an analytical sum model of spherical particles having a Schulz−Zimm distribution and hard spheres having a constant size of 0.6 nm in diameter (SAXS curves and corresponding fits are shown in Figure S4 in the Supporting Information). A detailed description of the fitting procedure of the model can be found in the Experimental Details. In the fitting, the size of the small silver structures was kept constant because small differences (i.e., ±0.1 nm) in this size regime are difficult to determine, in particular in the presence of the emerging nanoparticles. The resulting particle sizes are shown in Figure 6b, and it reveals that the particle size increases slightly with annealing temperature. At the annealing temperature of 450 °C the particle size distribution is hard to determine since the scattering of the small structures overlaps with the nanoparticle scattering. Thus, the sample annealed at 450 °C represents a state at which clusters ($d < 1$ nm) as well as nanoparticles with diameters of about 1 nm are present.

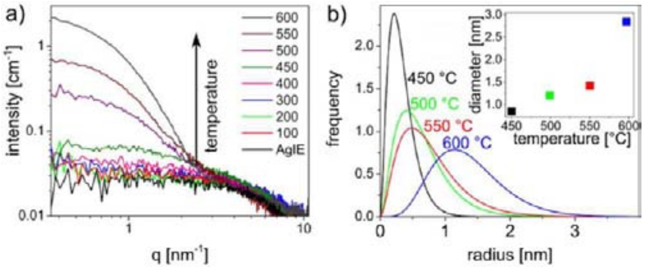

**Figure 6.** (a) SAXS curves of the silver samples annealed at different temperatures for 30 min. (b) Particle size distributions and determined mean particle sizes of the silver samples annealed above 400 °C.

TEM analysis of similarly prepared samples was carried out to show that the silver nanoparticles are of spherical shape. For TEM investigations the samples were prepared in the cross-sectional profile. The results deduced from the SAXS experiments (see Figure 6) are in accordance with the TEM analysis (Figure 7). The quantitative analysis of the size distribution histograms in the subnanometer regime reveals that with increasing temperature the fraction of particles with diameters less than 1 nm decreases (Figure 7b). In particular the number of clusters smaller than 0.5 nm in diameter decreases dramatically above 450 °C and even vanishes at 600 °C. Figure 7a shows a TEM picture of the 600 °C annealed Ag sample recorded with higher magnification. The clusters of about 0.5−0.9 nm size are marked with white circles. The TEM analysis of the formed nanoparticles yields a mean size and a standard deviation at 450 °C of 1.8 ± 1.1 nm (Figure 7c), at 500 °C of 1.9 ± 1.2 nm (Figure 7d), and at 600 °C of 2.2 ± 0.6 nm (see Figure 7e). The larger particles observed in TEM are

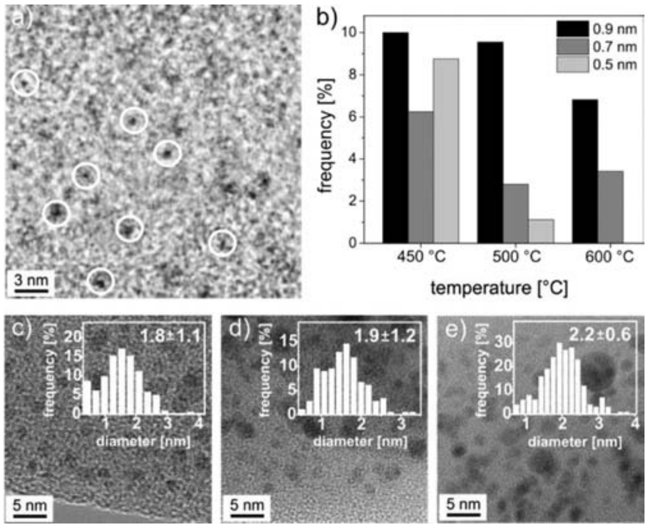

**Figure 7.** (a) TEM image of small silver clusters, recorded with 115.000× magnification. White circles mark the small clusters <1 nm in diameter. (b) Histogram of the number of clusters with $d < 1$ nm vs temperature, as determined from TEM measurements. The clusters are grouped into three different intervals ($d < 0.5$ nm, 0.5 nm $< d <$ 0.7 nm, and 0.7 nm $< d <$ 0.9 nm). TEM images of Ag glass samples annealed for 30 min at (c) 450 °C, (d) 500 °C, and (e) 600 °C. The insets show the corresponding size distribution histograms and the determined mean particle size with standard deviation. The size distribution histograms were constructed by counting several hundred individual particles (250−500). This number was used to normalize the bars of the histograms. The sum over all bars is 100%.

most likely generated during the sample preparation or the actual TEM measurement.

The temperature-dependent investigations reveal a well-defined temperature threshold at 410 °C. Below this threshold value small silver clusters ($d < 1$ nm) are formed. Above the threshold value the silver clusters concentration decreases, and nanoparticles are growing. Apparently, growth of clusters and nanoparticles proceeds without any additional reducing agent. Silver ions must be reduced prior to the cluster or particle formation. A reduction mechanism must be considered which is responsible for the particle formation during annealing. Interestingly, growth to nanoparticles occurs only above the temperature threshold at 410 °C. At this temperature it is reported that$\equiv$silver oxide ($Ag_2O$) decomposes to metallic $Ag^0$ and to $O_2$.[62,63] Therefore the silver reduction could occur due to electrons extracted directly from atoms that are intrinsic to the glass, namely nonbridging oxygens (NBOs) via the following reactions:[32,64]

$$2(\equiv\mathrm{Si{-}O^{-}Ag^{+}}) \leftrightarrow \equiv\mathrm{Si{-}O{-}Si}\equiv + \mathrm{O^{-}} + (\mathrm{Ag_2})^{+} \tag{2}$$

$$\mathrm{O^{-}} + (\mathrm{Ag_2})^{+} \rightarrow 2\mathrm{Ag^0} + 0.5\mathrm{O_2} \tag{3}$$

The Ag−O units can be approximately described as silver oxide, $Ag_2O$, which leads to a simplification of eqs 2 and 3:

$$2\mathrm{Ag_2O} \rightarrow 4\mathrm{Ag^0} + \mathrm{O_2} \tag{4}$$

The thermal decomposition of silver oxide has been observed in various experimental studies in the temperature range of 100−490 °C.[65−69] In addition, these studies also state that in the low temperature region (100 °C) silver oxide decomposes partially and above 400 °C silver oxide completely decomposes to $Ag^0$ and $O_2$.

**Annealing for Different Durations below the Threshold Temperature.** In this section the formation of silver clusters by annealing the ion-exchanged samples below the temperature threshold is presented. After ion exchange the samples were annealed at 400 °C for different durations between 1 min and 13 h.

Integrated photoluminescence intensity of the silver−glass samples annealed at 400 °C for different durations are shown in Figure 8a. Annealing below the threshold value for extended durations leads to an increase of the PL intensity which is attributed to further cluster formation. After 12 h of annealing the PL intensity increases insignificantly, suggesting that the majority of silver species is present in the form of clusters.

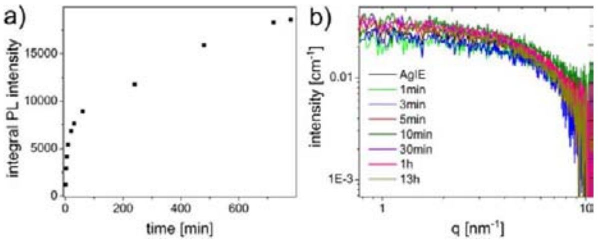

**Figure 8.** (a) Integral PL intensity and (b) SAXS curves of silver ion-exchanged samples annealed at 400 °C for different durations.

The samples annealed at 400 °C for different durations were investigated with SAXS (Figure 8b). The scattering curves are similar to those obtained for the ion-exchanged sample, and the intensity does not change with annealing duration. As the scattering intensity scales with $r^6$, the silver clusters must have dimensions similar to those of the silver ions. Hence, in accordance with the interpretation of Eichelbaum et al.[51] most probably silver dimers are forming during annealing below the threshold temperature. However, other molecular clusters might be present.

The silver samples annealed for 13 h at 400 °C, which exclusively contain silver clusters, were post-treated at 500 °C for different durations. SAXS curves of these samples are shown in Figure 9. It was observed that the scattering curves remained unchanged and silver nanoparticles are not forming even after 1 h heat treatment at 500 °C. Hence, the clusters formed during annealing below the temperature threshold (which are most likely silver dimers) are stable at elevated temperatures. This experiment clearly shows that Ostwald ripening is not happening.

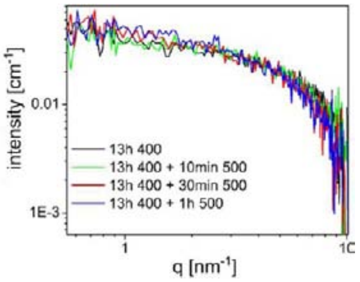

**Figure 9.** SAXS curves of silver samples annealed for 13 h at 400 °C and post-treated at 500 °C for different durations.

**Annealing for Different Durations above the Threshold Temperature.** In this section the influence of the annealing duration on the particle growth at constant annealing temperature is examined. After ion exchange the samples were annealed at 550 °C, above the threshold value, for different durations between 1 min and 16 h.

Absorption measurements reveal that the silver plasmon band with a maximum at around 420 nm evolves in the spectrum (Figure 10a). The plasmon band increases with longer duration which can be due to an increasing silver nanoparticle size or concentration.

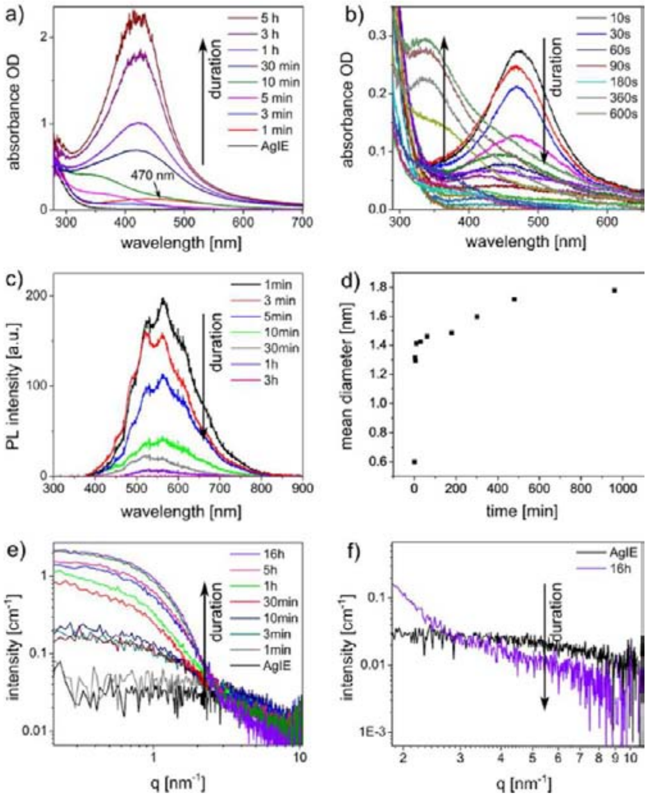

**Figure 10.** (a) Absorption spectra of silver samples annealed for different durations at 550 °C. (b) Absorption spectra recorded in situ in steps of 10 s during heating. The legend is given only for selected absorption spectra. (c) PL spectra, (d) mean particle diameter, and (e) SAXS scattering curves of the silver samples annealed for different durations at 550 °C. (f) SAXS curves of the silver ion-exchanged sample and the sample annealed 16 h at 550 °C.

Figure 10c shows the PL measurements that were conducted for the annealed silver glass samples. After longer annealing durations the PL intensity decreases and vanishes after 3 h of annealing at 550 °C due to a decrease of cluster concentration.

The samples annealed at 550 °C for different durations were investigated also with SAXS (Figure 10e). Fits to the SAXS curves are shown in the Supporting Information (see Figure S5). In accordance with the UV−vis measurements the SAXS investigations also reveal that particles larger than 1 nm in diameter are forming after 3 min of annealing. The arrow in Figure 10e indicates that the intensity of the SAXS curves increases systematically. With increasing annealing time the mean particle radius slightly increases and is 0.9 nm after 16 h (see Figure 10d) while the scattering at higher *q*-values caused by silver ions decreases (Figure 10f). From the model fitted to the SAXS curves it is possible to calculate also the volume fraction of nanoparticles compared to the total volume at each annealing time. The relatively high polydispersity as well as the coexistence of the small silver structures causes uncertainty. However, even a very high uncertainty of ~40−50% allows determining to which order of magnitude the volume fraction changes. The same applies for the particle concentration since it is related to the volume fraction and the particle size. The volume fraction of silver nanoparticles increases while the volume fraction of small silver structures decreases. After longer annealing times (8 h) the volume fraction of the silver nanoparticles reaches a plateau when the scattering of the silver ions is decreased by about 50%. Throughout the annealing process the concentration of formed particles does not change by more than 35%. Thus, it can be deduced that, in contrast to the increase of the volume fraction, the particle concentration remains constant. As a conclusion from the SAXS experiments, the number of the nanoparticles formed after 3 min of annealing is equal to the number of silver nanoparticles that grow after longer annealing durations (16 h).

After 1 min of annealing a broad band around 470 nm was observed in the absorption experiment. This band emerges in the first minutes of annealing decreases afterward and shifts to shorter wavelengths after 3 min of annealing (Figure 10a). This observation was examined more in detail by *in situ* UV−vis experiments using a tube furnace (Figure 10b). The ion-exchanged sample was placed in the middle of the tube furnace, and absorption was measured with the UV−vis setup as described in the Experimental Details. Absorption spectra were recorded every 10 s. After 10 s the band at 470 nm appears in the spectra.

This band decreases with further heat treatment and vanishes after 120 s when a temperature of approximately 400 °C is reached. After 180 s when approximately 500 °C is reached, the evolution of the silver plasmon band can be observed. The band at 470 nm which is an intermediate state of the silver nanoparticle formation most likely corresponds to an oxidic silver species.[63] Silver oxide is well-known to absorb in the spectral range of 450−500 nm.[62,63,70] The band at 470 nm could result from a separation of Ag−O units from the silver ions stabilized at the nonbonding oxygen atoms of the silanolate units[59−61] in the glass. The separated silver oxide can dissolve into metallic $Ag^0$ and $O_2$.

**Silver Particle Formation Mechanism.** The different stages of the particle formation process are summarized schematically in Figure 11. After the first synthetic step (ion exchange) the glass contains predominantly silver ions (that do not contribute to the PL) and few clusters. The PL intensity of the ion-exchanged sample is weak and increases when further molecular clusters are formed during annealing below the threshold temperature (410 °C). Annealing below the threshold value leads to the selective formation of clusters ($d$ < 1 nm) which are most likely silver dimers. With increasing annealing duration only the number of clusters increases. Furthermore, it was shown that these clusters/dimers remain stable at elevated temperatures (see Figure 9).

Thermal treatment above the threshold value leads to the growth of silver nanoparticles. The findings for annealing above the threshold temperature are the following: (i) the characteristic silver plasmon band evolves in the absorption spectra, (ii) the silver clusters (<1 nm) grow into larger nanoparticles, and hence, the number of clusters decreases (SAXS, TEM), (iii) the PL intensity (cluster concentration) decreases. Growth of (more stable) nanoparticles could proceed via an Ostwald ripening process.[71−76] Ostwald ripening occurs at temperatures matching the melting temperatures of the silver clusters. It is

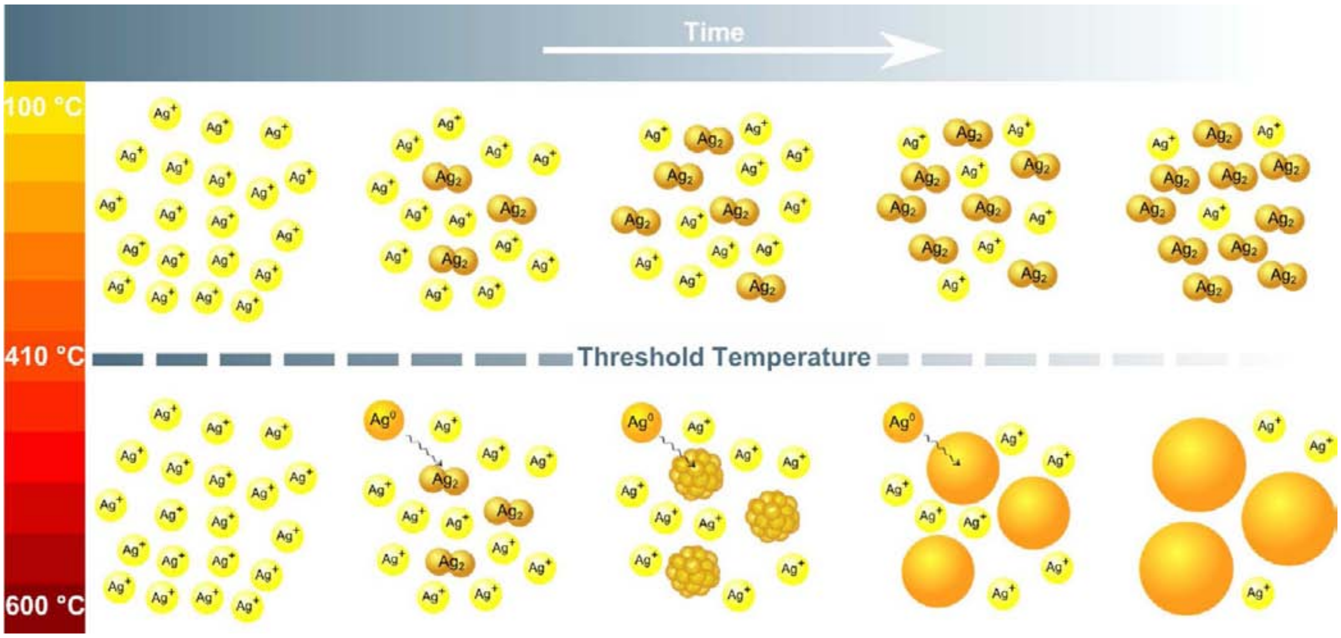

**Figure 11.** Schematic illustration of the initial steps of cluster formation and particle growth.

commonly known that the melting temperature scales with the materials dimensions.[77−83] However, it was found that the clusters remain stable at elevated temperatures. In addition, it was deduced that during annealing the number of particles remains constant and only the size is increasing. Even after longer annealing durations (16 h) the particle concentration equates the number of formed nanoparticles at the beginning of particle growth (after around 3 min). In contrast, Ostwald ripening processes would lead to a decrease in the number of particles.

The threshold temperature of 410 °C matches the decomposition temperature of silver oxide. The formation of intermediate silver oxide was observed as an initial step of cluster formation. According to eq 1, the silver atom formation by silver oxide decomposition comes along with the formation of bridging oxygen atoms from two nonbridging oxygens (NBOs). With this consideration, the environment of the forming silver particle is rearranged, and the number of available NBOs (reducing agent) is depleted. With the given glass composition (composition, wt %, $SiO_2$ 71.72, $Al_2O_3$ 1.23, $Fe_2O_3$ 0.19, $TiO_2$ 0.14, $SO_3$ 0.44, CaO 6.73, MgO 4.18, $Na_2O$ 14.95, $K_2O$ 0.34) one can estimate the number of oxygens in the form of NBOs. Bivalent cations require two NBOs and monovalent cations require one for charge balancing. The ratio of NBOs (of total oxygen content) is about 60% in the soda-lime silicate glass. Thus, the amount of silver atoms reduced by NBOs is limited by the number of available electrons from the glass matrix. From SAXS it was deduced that even after 16 h of thermal treatment (thus after particle formation) a substantial amount of silver ions (approximately 50% of the initial silver ion concentration) is still present in the samples.

The observations during the temperature dependent and duration dependent experiments suggest that the silver oxide decomposition in the low temperature regime proceeds differently than above the threshold value. The different observations below and above the temperature threshold (see Figure 11.) could be related to a different reduction mechanism or a different kinetic behavior of the silver oxide decomposition. At low temperatures (≤410 °C) the reduced silver species $Ag^0$ form only molecular clusters which are most likely silver dimers as indicated by the PL behavior. These small clusters are stable at elevated temperatures and do not dissolve. With annealing above the threshold temperature (>410 °C) the reduction rate increases, but further silver clusters are not formed. The existing clusters grow to nanoparticles via a monomer (silver atom) addition since the particle size increases with annealing duration but the particle concentration remains constant. The cluster formation in the initial step occurs during annealing below 410 °C as well as during the heating-up process in the beginning of annealing above 410 °C. In fact, the silver clusters act as nuclei and determine the number of resulting nanoparticles. Hence, the final particle size is determined by the cluster concentration formed in the initial step and the duration of annealing but is finally limited by the number of reducing agents (NBOs).

## ■ CONCLUSION

In this contribution, the growth mechanism of silver clusters and nanoparticles in glassy matrices was deduced. The findings show that the growth and thus the final size of the silver nanoparticles in soda-lime silicate glasses is determined by glass-intrinsic reduction mechanisms. Molecular clusters which are most likely silver dimers are formed in an initial step of particle formation and determine the final number of nanoparticles. These clusters grow by addition of silver monomers into nanoparticles. The final mean particle size is determined by the cluster concentration and the duration of annealing but is limited by the number of atoms acting as the reducing agent (NBOs). This is in contrast to several publications which assume that the nanoparticle formation is predominantly governed by Ostwald ripening processes.

## ■ EXPERIMENTAL DETAILS

**Synthesis.** Ion-exchanged glass samples were prepared from commercial soda-lime silicate glass slides of 1 mm thickness (composition, wt %, $SiO_2$ 71.72, $Al_2O_3$ 1.23, $Fe_2O_3$ 0.19, $TiO_2$ 0.14, $SO_3$ 0.44, CaO 6.73, MgO 4.18, $Na_2O$ 14.95, $K_2O$ 0.34). The glass slides, and the reagents of analytical grade $AgNO_3$ and $NaNO_3$ were purchased from Roth. The glass slides were cleaned with ethanol and stored in ethanol followed by rinsing with deionized water prior to use. Silver ion exchange was performed in a $AgNO_3/NaNO_3$ (1:2) salt bath at 360 °C for 60 min. Subsequently the ion-exchanged samples were annealed in air, varying temperature and duration. For details see main part of text.

**UV−Vis.** Optical absorption spectra of the as-exchanged and annealed samples were recorded in air at room temperature in the 200−1100 nm region (HR2000, Ocean Optics; Sony ILX511 CCD-detector, resolution (FWHW): 0.065 nm) with deuterium/tungsten lamp as the light source. Evaluation of the experimental data was done using Spectra Suite software (Ocean Optics). In situ UV−vis experiments were carried out using the same equipment and a tube furnace Heraeus (RO 4/25). The silver ion-exchanged sample was placed in the middle of the oven, and absorption spectra were collected every 10 s during the heat treatment (550 °C).

Luminescence emission spectra were recorded with the same equipment using a pulsed nitrogen laser MNL 103-PD (Lasertechnik Berlin, frequency 20 Hz, wavelength 337.1 nm, pulse energy 80 $\mu$J, pulse duration 3.5 ns) for excitation.

Photoluminescence excitation spectra were recorded in air at room temperature with a series 2 luminescence spectrometer (Aminco Bowman) equipped with a xenon lamp and a long pass filter in front of the output slit.

Photoluminescence lifetime measurements were conducted with TCSPC on a HORIBA Jobin YVON Fluorolog-3 Spectrofluorometer (V.1.2) in the standard configuration: double-grating monochromator in excitation and emission paths in "L" configuration, with a 450W-Xe lamp as light source and a PMT (CCD) detector. Data acquisition and manipulation were done with FluorEssenceTM software.

**TEM.** Size and structural identification of the formed clusters were performed by cross-sectional transmission electron microscopy (TEM; TITAN 80-300, FEI) with an acceleration voltage of 300 kV for Ag 1 min, Ag 30 min, and Ag 60 min annealed at 600 °C and CM200 FEG (Philips/FEI) with an acceleration voltage of 200 kV for Ag 30 min at 450 °C and Ag 30 min at 500 °C. The samples were prepared in the cross-section profile. Small pieces of the glass were sawed out and stick on a Si-dummy (3 mm × 0.5 mm × 0.5 mm) with epoxy. The resulting sandwich-preparation was thinned with SiC and diamond abrasive paper to a final thickness of 1 $\mu$m. The preparation was further thinned by Ar ion beam etching (PIPS, GATAN, 4 kV) to obtain the electron transparent material. Image plotting was done with Digital Micrograph. Statistical evaluation was done with ImageJ.

**ESEM.** Cross-sectional environmental scanning electron microscopy (ESEM) and energy dispersive X-ray spectroscopy (EDX) experiments were carried out on a tabletop microscope TM-1000 (Hitachi High-Technologies Europe GmbH) using a precentered cartridge filament electron gun and a high-sensitive semiconductor BSE (solid state backscattered electron) detector. The acceleration voltage was 15 kV and the obtained magnification was between 20 and 10.000x.

**SAXS.** Small-angle X-ray scattering and anomalous small-angle X-ray scattering was measured at beamline B1 of the DORIS III synchrotron storage at DESY, Hamburg. The measured SAXS curves have been background correted by subtracting the scattering of the pure soda-lime silicate glass. Throughout this paper we use the definition for the magnitude of scattering vector, $q = 4\pi\ \sin(\theta)/\lambda$. A Pilatus 1 M single-photon-counting pixel detector (Dectris) was used in all experiments. The SAXS measurements with a sample-to-detector distance of 883 mm were made at a photon energy of 16029 eV to have optimal transmission through the glass substrate. The beam size on the glass sample was 1 mm × 0.7 mm. Measurement time per sample was 100 to 300 s. The scattering curves of the silver containing glasses were analyzed assuming spherical shape, which is supported by TEM investigations (see Figure 8) and a homogeneous electron density. The experimental scattering curves were fitted using an analytical sum model of spherical particles having a Schulz−Zimm distribution and hard spheres. The Schulz−Zimm distribution is given by

$$f(x) = (z+1)^{z+1}x^{z}\ \frac{\exp[-(z+1)x]}{R_{\mathrm{avg}}\Gamma(z+1)} \tag{5}$$

where $R_{\mathrm{avg}}$ is the mean radius, $x = r/R_{\mathrm{avg}}$, $z$ is related to the polydispersity $p$ ($p = \sigma/R_{\mathrm{avg}}$) by $z = 1/p^2 - 1$, and $\sigma^2$ is the variance of the distribution. The mean particle volume can be calculated from the third moment of the size distribution leading to

$$V = \frac{4\pi}{3}R^3 = \frac{4\pi}{3}R_{\mathrm{avg}}{}^{3}\frac{(z+3)(z+2)}{(z+1)^2} \tag{6}$$

with $z$ defined as above. The scattering intensity of nonaggregated particles can be assumed to be proportional to the form factor of a single particle $P(q)$. Thus, the scattering intensity of monodisperse spheres with homogeneous electron density with volume $V_{part}$ is given by

$$I_{\mathrm{sphere}}(q) = NI_{\mathrm{part}}(q) = NV_{\mathrm{part}}^2P(q) = NV_{\mathrm{part}}^2 4\pi \times \left[\Delta\rho\frac{3(\sin(qR) - qR\cos(qR))}{qR}\right]^2 \tag{7}$$

In the case of polydisperse particles, one has to sum the scattering intensities over all particle sizes weighted by their frequency or to integrate using a size distribution function. Using the Schulz−Zimm distribution for polydisperse particles the scattering intensity is given by

$$I_{\mathrm{poly}}(q) = N\int_{\infty}^{0} f(r)V_{\mathrm{part}}^2P(q)\ \mathrm{d}r \tag{8}$$

An analytical solution of the integral can be found in Kotlarchyk et al.[84] The investigated samples contain small clusters with less than 1 nm in diameter and some of the annealed samples contain also nanoparticles. Thus, for the analysis of the SAXS scattering curve a mathematical model is applied which is the sum of the single sphere model ($I_{sphere}(q)$) and the polydisperse sphere model ($I_{\mathrm{poly}}(q)$). The number of particles can be obtained by using the general relation of $I_{\mathrm{sphere}}(q = 0)$ for a single particle, which is independent of its shape and size, that is $I = (\Delta\rho)^2V^2$. Thus, the scattered intensity $I_{\mathrm{poly}}(q = 0)$ of polydisperse particles can be written as

$$I_{\mathrm{poly}}(q = 0) = NV^2(\Delta\rho)^2 \tag{9}$$

where $N$ is the number of particles and $\langle V^2\rangle$ the mean value of $V^2$. Hence, the sum model contains information about the particle size and concentration of clusters as well as the nanoparticles. Selected scattering curves and their corresponding fits (model function) are given in the Supporting Information (S4 and S5).

**ASAXS.** Anomalous small-angle X-ray scattering gives element specific structural information.[85] The scattering length density $\rho$ of an element depends on the atomic scattering factor, which at low scattering angles can be expressed

$$f(E) = Z + f'(E) + if''(E) \tag{10}$$

where $Z$ is the atomic number and $f'$ and $f''$ are anomalous scattering coefficients which change rapidly close to an absorption edge of an element. Therefore, by measuring at different energies close to the edge, contrast variation of this element can be obtained. The ASAXS measurements were made at three different photon energies 25051, 25460, and 25509 eV, all below the Ag absorption K-edge which is at 25516 eV. Sample-to-detector distance was 883 mm and the total measurement time was about three hours.

The obtained SAXS and ASAXS images were normalized by the sample transmission, corrected for background scattering, integrated over the azimuth angle, and normalized onto the absolute intensity scale using a glassy carbon reference sample measurement. From SAXS curves (but not ASAXS curves) the scattering from a blank glass without Ag ions was subtracted. Data measured at different sample-to-detector distances were united to cover a larger $q$-range.

## ASSOCIATED CONTENT

### Ⓢ Supporting Information

Additional text, five figures, and two tables providing experimental details of the PL properties and SAXS fits with corresponding parameter results. This material is available free of charge via the Internet at http://pubs.acs.org.

## AUTHOR INFORMATION

### Corresponding Author

klaus.rademann@chemie.hu-berlin.de

### Notes

The authors declare no competing financial interest.

## ACKNOWLEDGMENTS

We are grateful to Achim Klein-Hoffmann and Prof. Robert Schlögl (FHI Berlin) for the TEM sample preparation. We thank Ning Da and Prof. Lothar Wondraczek (University Erlangen-Nürnberg) for the PL lifetime measurements. Parts of this research were carried out at the light source DORIS III at DESY, a member of the Helmholtz Association (HGF). This project was supported financially by Deutsche Forschungsgemeinschaft (RA-494 16/1, RA 464 17/1).

## REFERENCES

(1) Rao, C. N. R.; Cheetham, A. K. *J. Mater. Chem.* **2001**, *11*, 2887−2894.

(2) Eghtedari, M.; Oraevsky, A.; Copland, J. A.; Kotov, N. A.; Conjusteau, A.; Motamedi, M. *Nano Lett.* **2007**, *7* (7), 1914−1918.

(3) Niemeyer, C. M. *Angew. Chem., Int. Ed.* **2001**, *40*, 4128−4158.

(4) Link, S.; El-Sayed, M. A. *Annu. Rev. Phys. Chem.* **2003**, *54*, 331−366.

(5) Crooks, R. M.; Zhao, M.; Sun, L.; Chechik, V.; Yeung, L. K. *Acc. Chem. Res.* **2001**, *34* (3), 181−190.

(6) Daniel, M. C.; Astruc, D. *Chem. Rev.* **2004**, *104* (1), 293−346.

(7) Treguer, M.; Rocco, F.; Lelong, G.; Le Nestour, A.; Cardinal, T.; Maali, A.; Lounis, B. *Solid State Sci.* **2005**, *7*, 812−818.

(8) Stepanov, A. L. *Rev. Adv. Mater. Sci.* **2011**, *27* (2), 115−145.

(9) Polte, J.; Erler, R.; Thünemann, A. F.; Sokolov, S.; Ahner, T. T.; Rademann, K.; Emmerling, F.; Krähnert, R. *ACS Nano* **2010**, *4* (2), 1076−1082.

(10) Polte, J.; Ahner, T. T.; Delissen, F.; Sokolov, S.; Emmerling, F.; Thünemann, A. F.; Krähnert, R. *J. Am. Chem. Soc.* **2010**, *132*, 1296−1301.

(11) Polte, J.; Tuaev, X.; Wuithschick, M.; Fischer, A.; Thuenemann, A. F.; Rademann, K.; Kraehnert, R.; Emmerling, F. *ACS Nano* **2012**, *6*, 5791−5802.

(12) Díez, I.; Ras, R. H. A. *Nanoscale* **2011**, *3*, 1963−1970.

(13) Eichelbaum, M.; Rademann, K. *Adv. Funct. Mater.* **2009**, *19*, 2045−2052.

(14) Lillich, M. P. *The Armor of Light: Stained Glass in Western France*; California Studies in the History of Art; University of California Press: Berkeley, CA, 1994; pp 1250−1325.

(15) Kunckel, J. *Ars Vitraria Experimentalis*; Oder Vollkommene Glasmacher-Kunst: Frankfurt, 1689.

(16) Araci, I. E.; Himmelhuber, R.; De Rose, C. T.; Luo, J. D.; Jen, A. K.-Y.; Norwood, R. A.; Peyghambarian, N. *Opt. Express* **2010**, *18* (20), 21038−21046.

(17) Stepanov, A. L. *Rev. Adv. Mater. Sci.* **2010**, *26* (1−2), 1−29.

(18) Borsella, E.; Cattaruzza, E.; De Marchi, G.; Gonella, F.; Mattei, G.; Mazzoldi, P.; Quaranta, A.; Battaglin, G.; Polloni, R. *J. Non-Cryst. Solids* **1999**, *245*, 122−128.

(19) Qiu, J. R.; Shirai, M.; Nakaya, T.; Si, J. H.; Jiang, X. W.; Zhu, C. S.; Hirao, K. *Appl. Phys. Lett.* **2002**, *81* (16), 3040−3042.

(20) Mazzoldi, P.; Arnold, G. W; Battaglin, G; Gonella, F.; Haglund, R. F. *J. Nonlinear Opt. Phys. Mater.* **1996**, *5* (2), 285−330.

(21) Royon, A.; Bourhis, K.; Bellec, M.; Papon, G.; Bousquet, B.; Deshayes, Y.; Cardinal, T.; Canioni, L. *Adv. Mater.* **2010**, *22* (46), 5282−5286.

(22) Singh, S. P.; Karmakar, B. *Plasmonics* **2011**, *6* (3), 457−467.

(23) Qu, S.; Zhang, Y.; Li, H.; Qiu, J.; Zhu, C. *Opt. Mater.* **2006**, *28* (3), 259−265.

(24) Epifani, M.; Giannini, C.; Tapfer, L.; Vasanelli, L. *J. Am. Ceram. Soc.* **2000**, *83* (10), 2385−2393.

(25) Schottner, G. *Chem. Mater.* **2001**, *13*, 3422−3435.

(26) De Marchi, G.; Mattei, G.; Mazzoldi, P.; Sada, C.; Miotello, A. *J. Appl. Phys.* **2002**, *92* (8), 4249−4254.

(27) Haglund, R. F., Jr. *Mater. Sci. Eng., A* **1998**, *253* (1−2), 275−283.

(28) Fukumi, K.; Chayahara, A.; Kadono, K.; Sakaguchi, T.; Horino, Y.; Miya, M.; Fujii, K.; Hayakawa, J.; Satou, M. *J. Appl. Phys.* **1994**, *75* (6), 3075−3080.

(29) Manikandan, D.; Mohan, S.; Magudapathy, P.; Nair, K. G. M. *Physica B* **2003**, *325*, 86−91.

(30) Ramaswamy, R. V.; Srivastava, R. *J. Lightwave Technol.* **1988**, *6* (6), 984−1002.

(31) Quaranta, A.; Rahman, A.; Mariotto, G.; Maurizio, C.; Trave, E.; Gonella, F.; Cattaruzza, E.; Gibaudo, E.; Broquin, J. E. *J. Phys. Chem. C* **2012**, *116*, 3757−3764.

(32) Debenedetti, P. G.; Stillinger, F. H. *Nature* **2001**, *410*, 259−267.

(33) Lichtenstein, L.; Büchner, C.; Yang, B.; Shaikhutdinov, S.; Heyde, M.; Sierka, M.; Wlodarczyk, R.; Sauer, J.; Freund, H.-J. *Angew. Chem., Int. Ed.* **2012**, *51* (2), 404−407.

(34) Gy, R. *Mater. Sci. Eng., B* **2008**, *149* (2), 159−165.

(35) Karasinski, P. *Opto-Electron. Rev.* **2011**, *19* (1), 1−9.

(36) Maurizio, C.; Quaranta, A.; Ghibaudo, E.; D'Acapito, F.; Broquin, J.-E. *J. Phys. Chem. C* **2009**, *113*, 8930−8937.

(37) Kassab, L. R .P.; Bomfim, F. A.; Martinelli, J. R.; Wetter, N. U.; Neto, J. J.; de Araújo, C. B. *Appl. Phys. B* **2009**, *94*, 239−242.

(38) da Silva, D. M.; Kassab, L.R. P.; Lüthi, S. R.; de Araújo, C. B.; Gomes, A. S. L.; Bell, M. J. V. *Appl. Phys. Lett.* **2007**, *90*, 081913.

(39) Simo, A.; Joseph, V.; Fenger, R.; Kneipp, J.; Rademann, K. *Chem. Phys. Chem.* **2011**, *12* (9), 1683−1688.

(40) Sakka, S.; Kamiya, K.; Kato, K. *J. Non-Cryst. Solids* **1982**, *52* (1−3), 77−90.

(41) Loginov, E.; Gomez, L. F.; Chiang, N.; Halder, A.; Guggemos, N.; Kresin, V. V.; Vilesov, A. F. *Phys. Rev. Lett.* **2011**, *106*, 233401.

(42) Ozin, G. A.; Huber, H. *Inorg. Chem.* **1978**, *17*, 155−163.

(43) Petty, J. T.; Zheng, J.; Hud, N. V.; Dickson, R. M. *J. Am. Chem. Soc.* **2004**, *126*, 5207−5212.

(44) Harb, M.; Rabilloud, F.; Simon, D. *J. Phys. B: At. Mol. Opt. Phys.* **2011**, *44*, 035101 (7pp).

(45) Tomozawa, M., Doremus, R. H., Eds. *Treatise on Materials Science and Technology: Glass II*; Academic Press: New York, 1979; Vol. *17*.

(46) de Lamaestre, R. E.; Béa, H.; Bernas, H.; Belloni, J.; Marignier, J. L. *Phys. Rev. B* **2007**, *76* (20), 205431.

(47) Zheng, J.; Dickson, R. M. *J. Am. Chem. Soc.* **2002**, *124*, 13982−13983.

(48) Rao, T. U. B.; Pradeep, T. *Angew. Chem., Int. Ed.* **2010**, *49*, 3925−3929.

(49) Roy, S.; Banerjee, A. *Soft Matter* **2011**, *7*, 5300−5308.

(50) De Cremer, G.; Coutino-Gonzalez, E.; Roeffaers, M. B. J.; Moens, B.; Ollevier, J.; Van der Auweraer, M.; Schoonheydt, R.; Jacobs, P. A.; De Schryver, F. C.; Hofkens, J.; De Vos, D. E.; Sels, B. F.; Vosch, T. *J. Am. Chem. Soc.* **2009**, *131*, 3049−3056.

(51) Eichelbaum, M.; Rademann, K.; Hoell, A.; Tatchev, D. M.; Weigel, W.; Stößer, R.; Pacchioni, G. *Nanotechnology* **2008**, *19*, 135701.

(52) Tikhomirov, V. K.; Vosch, T.; Fron, E.; Rodriguez, V. D.; Velázquez, J. J.; Kirilenko, D.; Van Tendeloo, G.; Hofkens, J.; Van der Auweraer, M.; Moshchalkov, V. V. *RSC Adv.* **2012**, *2*, 1496−1501.

(53) De Cremer, G.; Antoku, Y.; Roeffaers, M. B. J.; Sliwa, M.; Van Noyen, J.; Smout, S.; Hofkens, J.; De Vos, D. E.; Sels, B. F.; Vosch, T. *Angew. Chem., Int. Ed.* **2008**, *47*, 2813−2816.

(54) Karthikeyan, B. *J. Appl. Phys.* **2008**, *103*, 114313.
(55) Paje, S. E.; Llopis, J.; Villegas, M. A.; Fernández Navarro, J. M. *Appl. Phys. A* **1996**, *63*, 431−434.
(56) Kreibig, U. *Z. Phys. D* **1986**, *3*, 239−249.
(57) Pedersen, J. S. *Adv. Colloid Interface Sci.* **1997**, *70*, 171−210.
(58) Jansen, M. *Angew. Chem.* **1987**, *99*, 1136−1149.
(59) Yang, X. C.; Li, W. J.; Dubiel, M.; Huang, W. H.; Yano, T. *J. Nanosci. Nanotechnol.* **2009**, *9* (2), 1659−1662(4).
(60) Houde-Walter, S. N.; Inman, J. M.; Dent, A. J.; Greaves, G. N. *J. Phys. Chem.* **1993**, *97*, 9330−9336.
(61) Dubiel, M.; Brunsch, S.; Kolb, U.; Gutwerk, D.; Bertagnolli, H. *J. Non-Cryst. Solids* **1997**, *220*, 30−44.
(62) Chiu, Y.; Rambabu, U.; Hsu, M.-H.; Shieh, H.-P. D.; Chen, C.-Y.; Lin, H.-H. *J. Appl. Phys.* **2003**, *94* (3), 1996−2001.
(63) Kipke, A.; Hofmeister, H. *Mater. Chem. Phys.* **2008**, *111*, 254−259 and references therein.
(64) Wackerow, S.; Seifert, G.; Abdolvand, A. *Opt. Mater. Express* **2011**, *1* (7), 1224−1231.
(65) L̀vov, B. V. *Thermochim. Acta* **1999**, *333*, 13−19.
(66) Herley, P. J.; Prout, E. G. *J. Am. Chem. Soc.* **1960**, *82* (7), 1540−1543.
(67) Garner, W. E.; Reeves, L. W. *Trans. Faraday Soc.* **1954**, *50*, 254−260.
(68) Weaver, J. F.; Hoflund, G. B. *Chem. Mater.* **1994**, *6*, 1693−1699.
(69) Weaver, J. F.; Hoflund, G. B. *J. Phys. Chem.* **1994**, *98*, 8519−8524.
(70) Varkey, A. J.; Fort, A. F. *Sol. Energ. Mater. Sol. C* **1993**, *29*, 253−259.
(71) Tatchev, D.; Hoell, A.; Eichelbaum, M.; Rademann, K. *Phys. Rev. Lett.* **2011**, *106*, 085702.
(72) Yata, K.; Yamaguchi, T. *J. Mater. Sci* **1992**, *27*, 101−106.
(73) Rizza, G.; Cheverry, H.; Gacoin, T.; Lamasson, A.; Henry, S. *J. Appl. Phys.* **2007**, *101*, 014321.
(74) De Marchi, G.; Mattei, G.; Mazzoldi, P.; Sada, C.; Miotello. *J. Appl. Phys.* **2002**, *92* (8), 4249−4254.
(75) Jiménez, J. A.; Sendova, M.; Senodva-Vassileva, M. *ACS Appl. Mater. Interfaces* **2011**, *3*, 447−454.
(76) Fukumi, K.; Chayahara, A.; Kadono, K.; Sakaguchi, T.; Horino, Y.; Miya, M.; Fujii, K.; Hayakawa, J.; Satou, M. *J. Appl. Phys.* **1994**, *75* (6), 3075−3080.
(77) Sun, C. Q. *Prog. Solid State Chem.* **2007**, *35*, 1−159.
(78) Cleveland, C. L.; Luedtke, W. D.; Landmann, U. *Phys. Rev. B* **1999**, *60* (7), 5065−5077.
(79) Lu, H. M.; Li, P. Y.; Cao, Z. H.; Meng, X. K. *J. Phys. Chem C* **2009**, *113*, 7598−7602.
(80) Nanda, K. K.; Sahu, S. N.; Behera, S. N. *Phys. Rev. A* **2002**, *66*, 013208.
(81) Castro, T.; Reifenberger, R.; Choi, E.; Andres, R. P. *Phys. Rev. B* **1990**, *42* (13), 8548−8556.
(82) Shyjumon, I.; Gopinadhan, M.; Ivanova, O.; Quaas, M.; Wulff, H.; Helm, C. A.; Hippler, R. *Eur. Phys. J. D* **2006**, *37*, 409−415.
(83) Little, S. A.; Begou, T.; Collins, R. W.; Marsillac, S. *Appl. Phys. Lett.* **2012**, *100*, 051107.
(84) Kotlarchyk, M.; Chen, S. H. *J. Chem. Phys.* **1983**, *79*, 2461−2469.
(85) Goerigk, G.; Haubold, H.-G.; Lyon, O.; Simon, J.-P. *J. Appl. Crystallogr.* **2003**, *36*, 425−429.